Propagation-inside-layer-expansion method combined with physical optics for scattering by coated cylinders, a rough layer, and an object below a rough surface

Christophe Bourlier,[1,*] Nicolas Pinel,[1] and Gildas Kubické[2]

[1]*IETR Laboratory, LUNAM Université, Université de Nantes, Polytech Nantes, Rue Christian Pauc, La Chantrerie, BP 50609, 44306 Nantes Cedex 3, France*

[2]*DGA Information Superority, CN1 Division, Bruz, France*

**Corresponding author: christophe.bourlier@univ-nantes.fr*

Received March 29, 2013; revised June 6, 2013; accepted July 3, 2013; posted July 8, 2013 (Doc. ID 188022); published August 5, 2013

In this article, the fields scattered by coated cylinders, a rough layer, and an object below a rough surface are computed by the efficient propagation-inside-layer-expansion (PILE) method combined with the physical optics (PO) approximation to accelerate the calculation of the local interactions on the non-illuminated scatterer, which is assumed to be perfectly conducting. The PILE method is based on the method of moments, and the impedance matrix of the two scatterers is then inverted by blocks from a Taylor series expansion of the inverse of the Schur complement. Its main interest is that it is rigorous, with a simple formulation and a straightforward physical interpretation. In addition, one of the advantages of PILE is to be able to hybridize methods (rigorous or asymptotic) valid for a single scatterer. Then, in high frequencies, the hybridization with PO allows us to significantly reduce the complexity in comparison to a direct lower–upper inversion of the impedance matrix of the two scatterers without loss in accuracy.

OCIS codes: (000.3860) Mathematical methods in physics; (050.1940) Diffraction; (260.0260) Physical optics; (290.5880) Scattering, rough surfaces.

http://dx.doi.org/10.1364/JOSAA.30.001727

1. INTRODUCTION

In this article, the field scattered by two objects, one of which is not directly illuminated, is computed. For instance, this general issue concerns the scattering from a coated object, from a stack of two rough interfaces of infinite lengths separating homogeneous media (rough layer), or from an object below a rough surface of infinite length (see Fig. 1). Numerically, it is not possible to generate a surface of infinite length. "Infinite length" means that the surface is large enough for both the incident field and the surface currents on the edges to vanish.

The applications of this general issue are numerous, and it is not possible to present an exhaustive review. See [1–16] (and references therein) for a partial review and also [5,10] for the scattering from objects in the presence of more than one interface. For instance, as shown in [15], the scattering from a dielectric elliptical cylinder, which is coated eccentrically by a nonconfocal dielectric elliptical cylinder, can be solved by introducing the Mathieu functions and the equivalent of the Graf theorem on the Bessel functions (used for circular cylinders). Nevertheless, the complexity of programing increases in comparison to the scattering from a circular coated cylinder. For the scattering from a rough layer or an object below a rough surface, there is no rigorous analytical solution, and then simplifying assumptions are introduced to solve the problem analytically. For example, see [2,12,16].

Then, to treat any geometry and any incident field, the method of moments (MoM) can be applied, which requires inverting the impedance matrix. If the scatterer is electrically large (high frequencies) and/or the relative permittivity (modulus) is large in comparison to one, the number of unknowns increases significantly, and then the inversion of the impedance matrix is very time consuming or sometimes even impossible. To solve this issue, it is then necessary to develop numerical methods called "rapid." For the scattering from two scatterers, a possible candidate is the versatile propagation-inside-layer-expansion (PILE) method [4]. It has the main advantage that the resolution of the linear system (obtained from the MoM) is broken up into different steps. Two steps are dedicated to solve the local interactions (computed by inverting a matrix), which can be done by efficient methods valid for a single rough interface, such as forward–backward (FB) [17–20] [complexity $\mathcal{O}(N^2)$], its accelerated version FB spectral acceleration (FB-SA) [21–24] [complexity $\mathcal{O}(N)$], and banded-matrix-iterative-approach/canonical grid (BMIA-CAG) [25–27] [complexity $\mathcal{O}(N \log N)$]. Two steps are dedicated to solve the coupling interactions (computed from a vector–matrix product), which can be done by updating the previous efficient methods. This has been investigated with BMIA/CAG [6] and FB-SA [7] for a rough layer, and by Bourlier *et al.* [8] for an object located below a rough surface, in which FB-SA is applied to calculate the local interactions on the rough surface. In the same spirit, PILE bas been extended (and named the E-PILE method) to treat the more general case of the scattering from two *illuminated* scatterers [28,29]. For the scattering from a perfectly conducting (PC) object above a rough sea surface, to accelerate the computation of the local interactions on the object, the physical optics

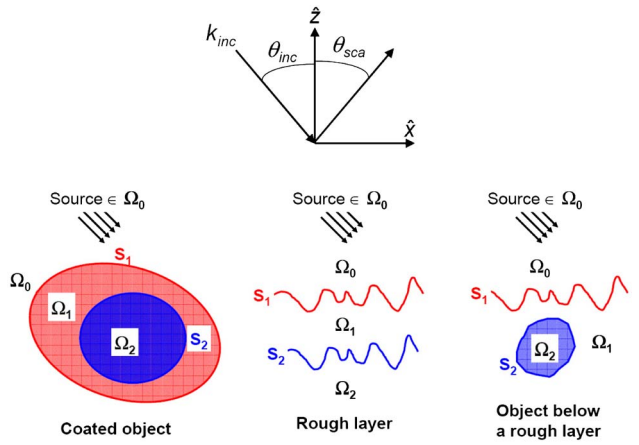

Fig. 1. Scattering from two scatterers where only one is illuminated. The source (incident field) is defined in medium Ω_0.

(PO) approximation bas been applied [30]. For this former case, the object was embedded in vacuum, unlike the case studied here, for which the object is below a dielectric rough surface.

The purpose of this paper is to combine PILE with PO and to test the validity of this hybridization on the geometries shown in Fig. 1. It is important to note that PILE has never been tested on a coated cylinder. The paper is organized as follows. Section 2 presents the PILE method and validates it by comparing the radar cross section (RCS) with that obtained analytically for a coated circular cylinder by introducing the Bessel functions. Section 3 explains how PILE can be combined with PO, studies the validity of this new method, and presents numerical results. Section 4 gives concluding remarks and prospects.

2. PILE METHOD

In this section, the PILE method is briefly presented from [4,6–8].

A. Impedance Matrix $\bar{\boldsymbol{Z}}$

From the boundary integral equations, the surface currents ψ_i and $\partial\psi_i/\partial n$ on each scatterer i ($i=\{1,2\}$) must be determined. From the MoM, the boundary integral equations are discretized on each surface of the scatterer, leading to the linear system $\bar{\boldsymbol{Z}}\boldsymbol{X}=\boldsymbol{b}$. The unknown vector is then

$$\boldsymbol{X}=\begin{bmatrix}\boldsymbol{X}_1\\ \boldsymbol{X}_2\end{bmatrix}, \tag{1}$$

where the components of the vectors $\boldsymbol{X}_1$ and $\boldsymbol{X}_2$ are the surface currents discretized on the surfaces S_1 and S_2, respectively. They are written as

$$\boldsymbol{X}_1=\left[\psi_1(\boldsymbol{r}_1)\ldots\psi_1(\boldsymbol{r}_{N_1})\quad \frac{\partial\psi_1(\boldsymbol{r}_1)}{\partial n}\ldots\frac{\partial\psi_1(\boldsymbol{r}_{N_1})}{\partial n}\right]^T,\ \boldsymbol{r}_{p_{\in[1;N_1]}}\in S_1, \tag{2}$$

$$\boldsymbol{X}_2=\left[\psi_2(\boldsymbol{r}_1)\ldots\psi_2(\boldsymbol{r}_{N_2})\quad \frac{\partial\psi_2(\boldsymbol{r}_2)}{\partial n}\ldots\frac{\partial\psi_2(\boldsymbol{r}_{N_2})}{\partial n}\right]^T,\ \boldsymbol{r}_{p_{\in[1;N_2]}}\in S_2, \tag{3}$$

where the symbol T stands for the transpose operator and N_i is the number of samples on the surface S_i. Then the length of the vector $\boldsymbol{X}_i$ is $2N_i$.

The vector $\boldsymbol{b}$ of length $2(N_1+N_2)$ is the incident field discretized on the surface S_i. It is defined as

$$\boldsymbol{b}=\begin{bmatrix}\boldsymbol{b}_1\\ \boldsymbol{b}_2\end{bmatrix}=\left[\underbrace{\psi_{\text{inc}}(\boldsymbol{r}_1)\ldots\psi_{\text{inc}}(\boldsymbol{r}_{N_1})}_{\mathbf{b}_1^T,\boldsymbol{r}\in S_1}\ \underbrace{0\ldots0}_{N_1\ \text{times}}\quad \underbrace{0\ldots0}_{2N_2\ \text{times}}\right]^T. \tag{4}$$

The impedance matrix $\bar{\boldsymbol{Z}}$ of size $2(N_1+N_2)\times2(N_1+N_2)$ is expressed as

$$\bar{\boldsymbol{Z}}=\begin{bmatrix}\bar{\boldsymbol{A}}_1 & \bar{\boldsymbol{B}}_1 & \bar{\mathbf{0}} & \bar{\mathbf{0}}\\ \bar{\boldsymbol{C}}_1 & \frac{1}{\rho_{01}}\bar{\boldsymbol{D}}_1 & \bar{\boldsymbol{A}}_{21} & \bar{\boldsymbol{B}}_{21}\\ \bar{\boldsymbol{A}}_{12} & \frac{1}{\rho_{01}}\bar{\boldsymbol{B}}_{12} & \bar{\boldsymbol{A}}_2 & \bar{\boldsymbol{B}}_2\\ \bar{\mathbf{0}} & \bar{\mathbf{0}} & \bar{\boldsymbol{C}}_2 & \frac{1}{\rho_{12}}\bar{\boldsymbol{D}}_2\end{bmatrix}=\begin{bmatrix}\bar{\boldsymbol{Z}}_1 & \bar{\boldsymbol{Z}}_{21}\\ \bar{\boldsymbol{Z}}_{12} & \bar{\boldsymbol{Z}}_2\end{bmatrix}, \tag{5}$$

where

$$\bar{\boldsymbol{Z}}_1=\begin{bmatrix}\bar{\boldsymbol{A}}_1 & \bar{\boldsymbol{B}}_1\\ \bar{\boldsymbol{C}}_1 & \frac{1}{\rho_{01}}\bar{\boldsymbol{D}}_1\end{bmatrix},\qquad \bar{\boldsymbol{Z}}_2=\begin{bmatrix}\bar{\boldsymbol{A}}_2 & \bar{\boldsymbol{B}}_2\\ \bar{\boldsymbol{C}}_2 & \frac{1}{\rho_{12}}\bar{\boldsymbol{D}}_2\end{bmatrix}, \tag{6}$$

and

$$\bar{\boldsymbol{Z}}_{21}=\begin{bmatrix}\bar{\mathbf{0}} & \bar{\mathbf{0}}\\ \bar{\boldsymbol{A}}_{21} & \bar{\boldsymbol{B}}_{21}\end{bmatrix},\qquad \bar{\boldsymbol{Z}}_{12}=\begin{bmatrix}\bar{\boldsymbol{A}}_{12} & \frac{1}{\rho_{01}}\bar{\boldsymbol{B}}_{12}\\ \bar{\mathbf{0}} & \bar{\mathbf{0}}\end{bmatrix}. \tag{7}$$

The impedance matrix $\bar{\boldsymbol{Z}}_i$ of size $2N_i\times2N_i$ is the impedance matrix of the single scatterer i, where N_i is the number of samples on scatterer i. Moreover, matrices $\bar{\boldsymbol{Z}}_{21}$ of size $2N_1\times2N_2$ (propagation from scatterer 2 to 1) and $\bar{\boldsymbol{Z}}_{12}$ of size $2N_2\times2N_1$ (propagation from scatterer 1 to 2) are coupling matrices between scatterers 1 and 2. The expressions of the elements of matrices $\bar{\boldsymbol{Z}}_i$ and $\bar{\boldsymbol{Z}}_{ij}$ ($i=\{1,2\}$ and $j=\{1,2\}\neq i$) are reported in Appendix A. $\rho_{ij}=1$ ($i=\{0,1\}$ and $j=\{1,2\}\neq i$) for the TE polarization and $\rho_{ij}=\varepsilon_i/\varepsilon_j$ for the TM polarization, where ε_i is the permittivity of medium Ω_i. Appendix B simplifies the matrices when scatterer 2 is PC.

B. Scattered Field and RCS

From the knowledge of the surface currents $\{\psi_i,\partial\psi_i/\partial n\}$ on the scatterers S_i ($i=\{1,2\}$), the scattered field $\psi_{\text{sca},\nu}$ inside the medium Ω_ν ($\nu=\{0,1,2\}$) is computed from the Huygens principle as

$$\begin{cases} \psi_{\mathrm{sca},0}(\boldsymbol{r}') = \int_{S_1}\left[\psi_0(\boldsymbol{r})\frac{\partial g_0(\boldsymbol{r},\boldsymbol{r}')}{\partial n} - g_0(\boldsymbol{r},\boldsymbol{r}')\frac{\partial \psi_0(\boldsymbol{r})}{\partial n}\right]\mathrm{d}S \\ \psi_{\mathrm{sca},1}(\boldsymbol{r}') = \sum_{p=1}^{p=2} s_p \int_{S_p}\left[\psi_p(\boldsymbol{r})\frac{\partial g_1(\boldsymbol{r},\boldsymbol{r}')}{\partial n} - g_1(\boldsymbol{r},\boldsymbol{r}')\frac{\partial \psi_p(\boldsymbol{r})}{\partial n}\right]\mathrm{d}S, \\ \psi_{\mathrm{sca},2}(\boldsymbol{r}') = -\int_{S_2}\left[\psi_2(\boldsymbol{r})\frac{\partial g_2(\boldsymbol{r},\boldsymbol{r}')}{\partial n} - g_2(\boldsymbol{r},\boldsymbol{r}')\frac{\partial \psi_2(\boldsymbol{r})}{\partial n}\right]\mathrm{d}S \end{cases} \tag{8}$$

where $s_1 = -1$, $s_2 = +1$, and $g_\nu(\boldsymbol{r},\boldsymbol{r}') = (j/4)\mathrm{H}_0^{(1)}(k_\nu\|\boldsymbol{r}'-\boldsymbol{r}\|)$ is the zeroth-order Hankel function of the first kind.

In addition, the RCS in the medium Ω_0 is expressed as

$$\mathrm{RCS} = \lim_{r'\to\infty} 2\pi r'\left|\frac{\psi_{\mathrm{sca},0}}{\psi_{\mathrm{inc},0}}\right|^2 = \frac{|\psi^{\infty}_{\mathrm{sca},0}|^2}{4|k_0|}, \tag{9}$$

where k_0 is the wavenumber inside the medium Ω_0 and

$$\psi^{\infty}_{\mathrm{sca},0} = -\frac{1}{\psi_{\mathrm{inc},0}}\int_{S_1}\left[j\boldsymbol{k}_{\mathrm{sca}}\cdot\hat{\boldsymbol{n}}_0\psi_0(\boldsymbol{r}) + \frac{\partial\psi_0(\boldsymbol{r})}{\partial n}\right]e^{-j\boldsymbol{k}_{\mathrm{sca}}\cdot\boldsymbol{r}}\mathrm{d}S, \tag{10}$$

where $\psi_{\mathrm{inc},0}$ is the modulus of the incident field ψ_{inc} in the medium Ω_0. In addition, $\hat{\boldsymbol{n}}_0$ is the unitary vector normal to the surface pointed toward Ω_0.

To test the precision of the MoM, the RCS is compared with that obtained analytically for a coated circular cylinder by introducing Bessel functions. The derivation of this solution is summarized in Appendix C by assuming an incident plane wave defined in the medium Ω_0 by $\psi_{\mathrm{inc}} = \psi_{\mathrm{inc},0}e^{jk_0(x\sin\theta_{\mathrm{inc}} - z\cos\theta_{\mathrm{inc}})}$, where k_0 is the wavenumber and θ_{inc} is the incident angle defined from the vertical $\hat{z}$ (see Fig. 1). Figure 2 plots the RCS in decibel scale versus the scattering angle θ_{sca}. The radii of the two concentric circular cylinders are $a_1 = 3\lambda_0$ and $a_2 = 2\lambda_0$; their centers are $C_1 = C_2 = (0,0)$; the relative permittivities of media $\{\Omega_0,\Omega_1,\Omega_2\}$ are $\{\varepsilon_{r0} = 1, \varepsilon_{r1} = 2, \varepsilon_{r2} = 4 + 0.05j\}$, respectively; and the wavelength inside Ω_0 is $\lambda_0 = 1$ m. The incidence angle is $\theta_{\mathrm{inc}} = 0$ and the polarization is TE. For the MoM, the number of samples per wavelength is $N_{\lambda_0} = \{10, 20\}$, and in the legend, the number corresponds to the number of unknowns $2(N_1 + N_2)$. For a dielectric medium Ω_i, the number of samples per wavelength is $N_{\lambda_0}\sqrt{|\varepsilon_{ri}|}$, where ε_{ri} is the relative permittivity of medium i. Figure 3 plots the same results as in Fig. 2, but for the TM polarization. Figures 4 and 5 plot the ratio $\mathrm{RCS_{LU}}/\mathrm{RCS_{Analytical}}$ in decibels (difference in decibels) versus the scattering angle θ_{sca}. Figures 2 and 3 show a good agreement between the two methods, and as the number of unknowns increases, the difference slightly decreases. Figures 4 and 5 show that the differences increase when the RCS is very small, and they are smaller for the TM polarization.

Table 1 lists the computation time obtained from the MatLab software. For the analytical solution, the computation time is very small in comparison to that obtained from the MoM because the LU inversion of the impedance matrix is not required. As the number of unknown increases, the computation time increases because the size of the matrix to invert increases.

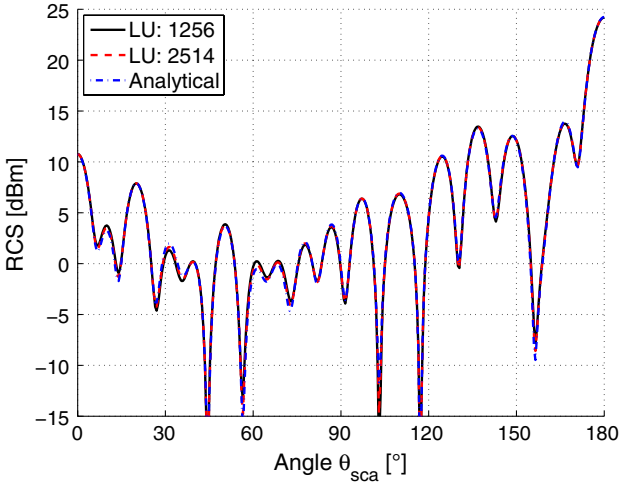

Fig. 2. RCS in decibel scale versus the scattering angle θ_{sca}. The radii of the two concentric circular cylinders are $a_1 = 3\lambda_0$ and $a_2 = 2\lambda_0$; their centers are $C_1 = C_2 = (0,0)$; the relative permittivities of media $\{\Omega_0,\Omega_1,\Omega_2\}$ are $\{\varepsilon_{r0} = 1, \varepsilon_{r1} = 2, \varepsilon_{r2} = 4 + 0.05j\}$, respectively; and the wavelength inside Ω_0 is $\lambda_0 = 1$ m. The incidence angle is $\theta_{\mathrm{inc}} = 0$, and the polarization is TE. For the MoM, the number of samples per wavelength is $N_{\lambda_0} = \{10, 20\}$.

C. Efficient Inversion of the Impedance Matrix

To efficiently solve the system $\bar{\boldsymbol{Z}}\boldsymbol{X} = \boldsymbol{b}$, the PILE method has been developed [4]. It is based on the inversion by blocks (series Taylor expansion of the inverse of the Schur complement [31]) of the impedance matrix. This leads to

$$\boldsymbol{X}_1 = \left[\sum_{p=0}^{p=P_{\mathrm{PILE}}}\bar{\boldsymbol{M}}_c^p\right]\bar{\boldsymbol{Z}}_1^{-1}\boldsymbol{b}_1 = \sum_{p=0}^{p=P_{\mathrm{PILE}}}\boldsymbol{Y}_1^{(p)}, \tag{11}$$

in which

$$\begin{cases} \boldsymbol{Y}_1^{(0)} = \bar{\boldsymbol{Z}}_1^{-1}\boldsymbol{b}_1 & \text{for } p = 0 \\ \boldsymbol{Y}_1^{(p)} = \bar{\boldsymbol{M}}_c\boldsymbol{Y}_1^{(p-1)} & \text{for } p > 0 \end{cases}, \tag{12}$$

and

$$\bar{\boldsymbol{M}}_c = \bar{\boldsymbol{Z}}_1^{-1}\bar{\boldsymbol{Z}}_{21}\bar{\boldsymbol{Z}}_2^{-1}\bar{\boldsymbol{Z}}_{12}. \tag{13}$$

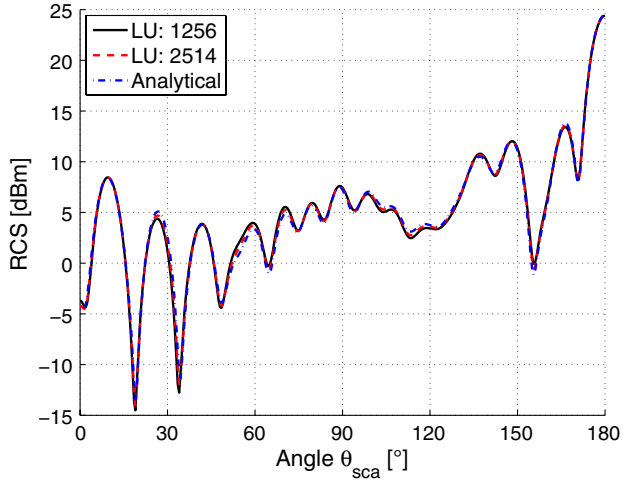

Fig. 3. Results for the same parameters as in Fig. 2, but for the TM polarization.

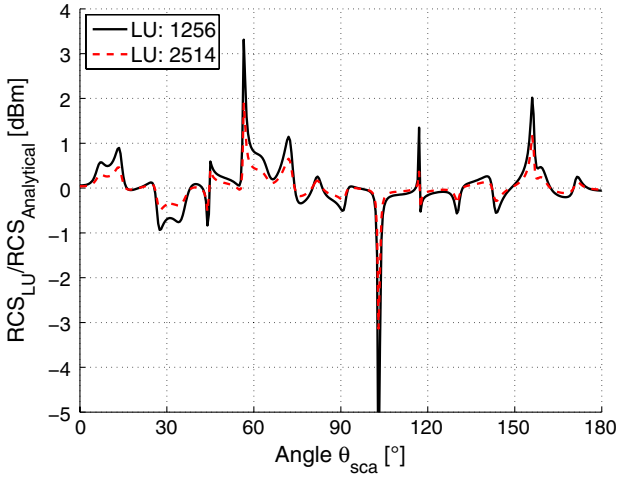

Fig. 4. Ratio $\mathrm{RCS_{LU}/RCS_{Analytical}}$ in decibels (difference in decibels) versus the scattering angle θ_{sca}. The parameters are the same as in Fig. 2.

In addition, $\boldsymbol{X}_2 = -\bar{\boldsymbol{Z}}_2^{-1}\bar{\boldsymbol{Z}}_{12}\boldsymbol{X}_1$. We define the norm $\|\bar{\boldsymbol{M}}_c\|$ of a complex matrix by its spectral radius, namely, the modulus of the eigenvalue which has the highest modulus. Expansion (11) is then valid if $\|\bar{\boldsymbol{M}}_c\|$ is strictly smaller than one.

Equation (12) has a clear physical interpretation: The total currents on scatterer 1 are the sum of the contributions $\boldsymbol{Y}_1^{(p)}$ corresponding to successive iterations p. In the zeroth-order term, $\bar{\boldsymbol{Z}}_1^{-1}$ accounts for the local interactions on scatterer 1, so $\boldsymbol{Y}_1^{(0)}$ corresponds to the contribution of the direct reflection on scatterer 1, without entering inside the medium Ω_1. In the first-order term given by $\boldsymbol{Y}_1^{(1)} = \bar{\boldsymbol{M}}_c\boldsymbol{Y}_1^{(0)}$, the matrix $\bar{\boldsymbol{Z}}_{12}$ propagates the resulting currents, $\boldsymbol{Y}_1^{(0)}$, toward scatterer 2, $\bar{\boldsymbol{Z}}_2^{-1}$ accounts for the local interactions on scatterer 2, and the matrix $\bar{\boldsymbol{Z}}_{21}$ repropagates the resulting contribution toward scatterer 1; finally, $\bar{\boldsymbol{Z}}_1^{-1}$ updates the surface current values on scatterer 1, and so on for the subsequent terms $\boldsymbol{Y}_1^{(p)}$ for $p > 1$. Thus, the total currents $\sum_p \boldsymbol{Y}_1^{(p)}$ on scatterer 1 correspond to the multiple scattering of the field inside the medium Ω_1. The surface heights are obtained from the convolution of a Gaussian white noise.

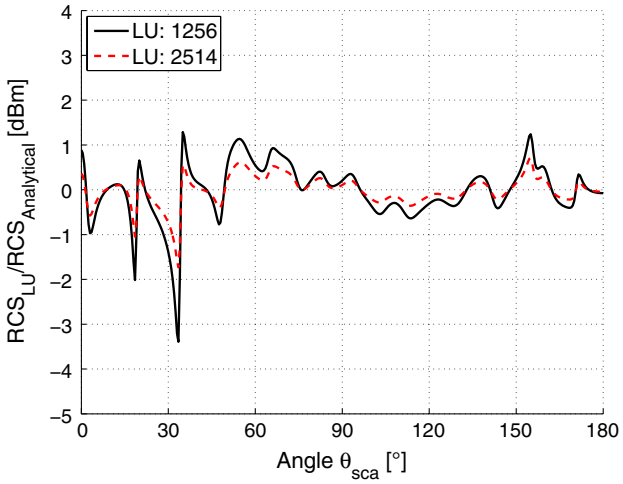

Fig. 5. Ratio $\mathrm{RCS_{LU}/RCS_{Analytical}}$ in decibels (difference in decibels) versus the scattering angle θ_{sca}. The parameters are the same as in Fig. 3.

Table 1. Computation Times in Seconds to Obtain the Results of Figs. 2 and 3

Polarization	LU, $N_{\lambda_0} = 10$	LU, $N_{\lambda_0} = 20$	Analytical
TM	1.67	5.80	0.02
TE	1.66	5.83	0.02

D. Numerical Results for the Three Scenarios

For the scattering from a rough surface, to simulate a surface of infinite length, both the incident field and the surface currents must vanish on the edges. Thus, the well-known tapered Thorsos wave is applied [32]. In addition, the normal RCS (NRCS) or the scattering coefficient is then [33]

$$\mathrm{NRCS}(\theta_{\mathrm{inc}},\theta_{\mathrm{sca}}) = \lim_{r'\to\infty}\frac{r'\|\boldsymbol{p}_{\mathrm{sca},0}\|}{P_{\mathrm{inc}}} = \frac{1}{16\pi\eta_0 k_0}\frac{|\psi^{\infty}_{\mathrm{sca},0}|^2}{P_{\mathrm{inc}}}, \quad (14)$$

where

$$P_{\mathrm{inc}} = \frac{g\cos\theta_{\mathrm{inc}}}{2\eta_0}\sqrt{\frac{\pi}{2}}\left[1-\frac{1+2\tan^2\theta_{\mathrm{inc}}}{2k_0^2 g^2\cos^2\theta_{\mathrm{inc}}}\right], \quad (15)$$

and $\eta_0 = 120\pi$ is the wave impedance in Ω_0. In addition, P_{inc} is the average incident power on the surface $z = 0$, $\boldsymbol{p}_{\mathrm{sca},0}$ is the Poynting vector of the scattered field, $\psi^{\infty}_{\mathrm{sca},0}$ is expressed from Eq. (10), and the parameter g controls the extent of the incident wave and typically equals $L/4$, where L is the surface length. Unlike the RCS (in meters for a two-dimensional problem), the NRCS is dimensionless.

Figure 7 plots the RCS (in dBm) or the NRCS (in dB) versus the scattering angle θ_{sca} for a coated elliptical cylinder, an elliptical cylinder below a rough surface, and a rough layer, respectively. The polarization is TE, and the parameters of the scenarios are given in the caption of Fig. 6. In the legend, for each PILE order, the number is the residual error, defined as

$$\varepsilon_{\mathrm{PILE}} = \frac{\mathrm{norm}_{\theta_{\mathrm{sca}}}(\mathrm{RCS_{PILE}} - \mathrm{RCS_{LU}})}{\mathrm{norm}_{\theta_{\mathrm{sca}}}(\mathrm{RCS_{LU}})}, \quad (16)$$

where the symbol "norm" is norm 2. The same definition is used for the NRCS. The subscript "LU" means that the impedance matrix is inverted from a direct LU inversion. Figure 7 shows that PILE converges rapidly. The order zero corresponds to the scattering from only the upper scatterer. Thus, PILE allows us to quantify the coupling between the two scatterers, which cannot be exhibited from a direct LU inversion. Values of the norm $\|\bar{\boldsymbol{M}}_c\|$ of the characteristic matrix defined by Eq. (13) is given in Table 2, for the TE and TM polarizations. For a detailed analysis of the PILE convergence, the reader is referred to [4] for a random rough layer and to [8] for an object below a random rough surface.

3. PILE COMBINED WITH PO

As shown previously, the first advantage of PILE in comparison to a direct LU inversion is the ability to quantify the coupling between the two scatterers. Equation (12) clearly shows that the calculation of $\bar{\boldsymbol{Z}}_i^{-1}\boldsymbol{u}$ is required, in which $\bar{\boldsymbol{Z}}_i$ is the impedance matrix of the scatterer i alone. Then, rapid methods developed for a single scatterer can be applied. This is the

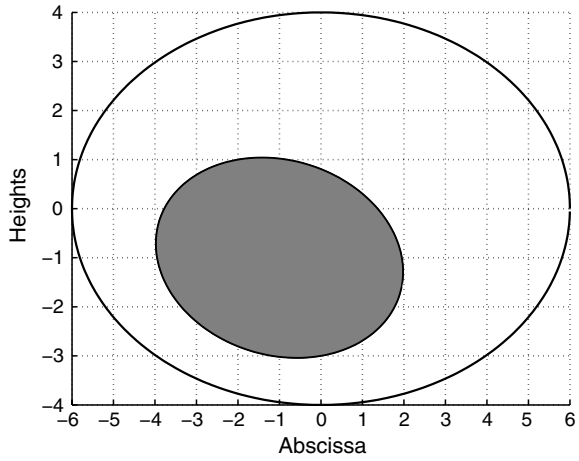

(a) Scenario 1 : Elliptical coated cylinder.

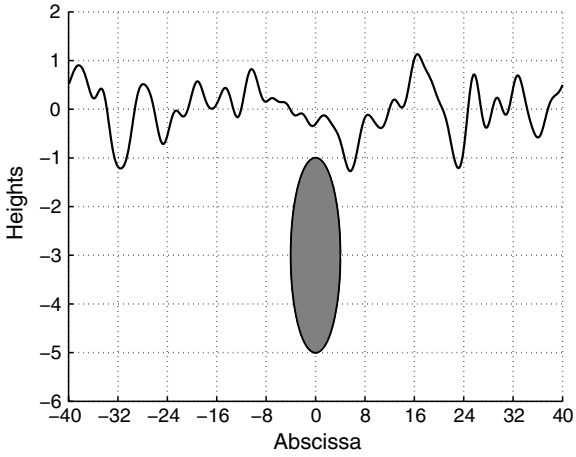

(b) Scenario 2 : Elliptical cylinder below a random rough surface.

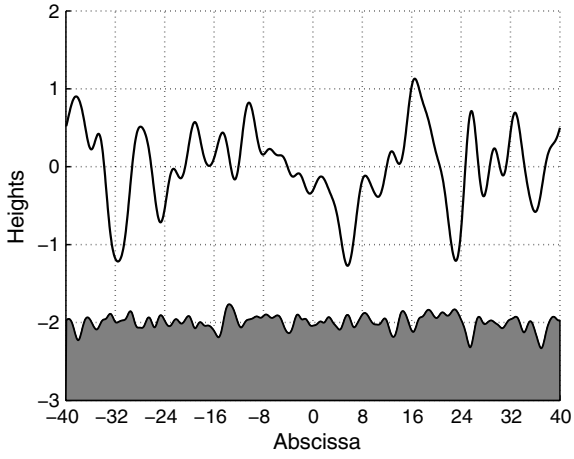

(c) Scenario 3 : Random rough layer.

Fig. 6. (a) Coated elliptical cylinder: semi-major axis $a_1 = 6\lambda_0$, $a_2 = 3\lambda_0$, semi-minor axis $b_1 = 4\lambda_0$, $b_2 = \lambda_0$, centers $C_1 = (0,0)$, $C_2 = (-1,-1)\lambda_0$, and rotation angles $\alpha_1 = 0$, $\alpha_2 = -10°$. (b) Elliptical cylinder below a rough surface: $a_2 = 4\lambda_0$, $b_2 = 2\lambda_0$, $C_2 = (0,-3)\lambda_0$, $\alpha_2 = 0$, surface length $L_1 = 80\lambda_0$, center $C_1 = (0,0)\lambda_0$, height standard deviation $\sigma_{z1} = 0.5\lambda_0$, correlation length $L_{c1} = 2\lambda_0$; the surface height autocorrelation function is Gaussian, and the parameter of the Thorsos wave is $g = L_1/4$. (c) Rough layer: $L_1 = L_2 = 80\lambda_0$, $\sigma_{z1} = 0.5\lambda_0$, $\sigma_{z2} = 0.1\lambda_0$, $L_{c1} = 2\lambda_0$, $L_{c2} = \lambda_0$, $C_1 = (0,0)\lambda_0$, $C_2 = (0,-2)\lambda_0$; the surface height autocorrelation function for both surfaces is Gaussian, and the parameter of the Thorsos wave is $g = L_1/4$. In addition; for the three scenarios, the incidence angle is $\theta_{\text{inc}} = 30°$, the relative permittivities of media $\{\Omega_0, \Omega_1, \Omega_2\}$ are $\{1, 2 + 0.1j, j\infty(\text{PC})\}$, and the total number of unknowns are $N = \{1047, 2434, 3040\}$, for scenarios (a), (b), and (c), respectively.

second advantage of PILE. For example, when the scatterer is a rough surface, to accelerate the computation of the local interactions, FB, FB-SA, or BMIA/CAG can be applied. For more details, see [6,7] for a rough layer and [8] for any scatterer below a rough surface. In addition, in [8], it was shown for FB that the order P_{FB} of convergence is obtained by considering only the scattering from the single rough surface (without the other scatterer). Physically, this point can be explained by the fact that the inversion of the impedance matrix is independent of the incident field $\boldsymbol{u}$.

For a closed surface, like an elliptical cylinder, FB, FB-SA, and BMIA-CAG do not converge. Then, to accelerate the calculation of the local interactions on a closed object, the PO approximation (also valid for a rough surface) can be combined with PILE. This is the purpose of this section.

A. PILE Combined with PO

For scatterer 2, which is assumed to be PC, the total field on the object surface in the medium Ω_1 due to a single reflection is given under the PO approximation by

$$\psi_2(\boldsymbol{r}) = 2\begin{cases} \psi_{\text{inc},1}(\boldsymbol{r}) & \boldsymbol{r} \in S_{2,\text{Ill}} \\ 0 & \boldsymbol{r} \in S_{2,\text{Sha}} \end{cases} \quad \text{and} \quad \frac{\partial \psi_2(\boldsymbol{r})}{\partial n} = 0 \,\forall\, S_2, \text{TM polarization}, \tag{17}$$

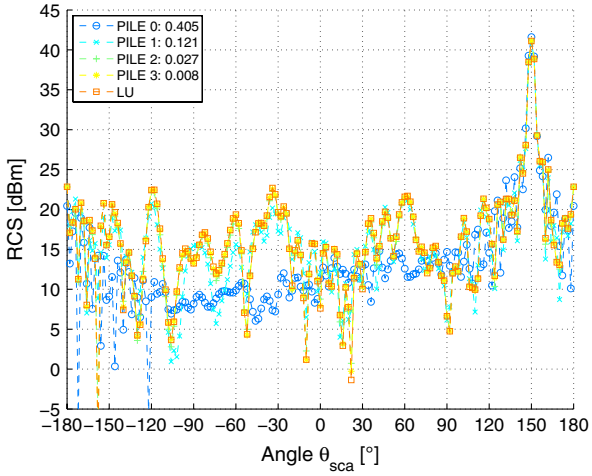

(a) Scenario 1 : RCS.

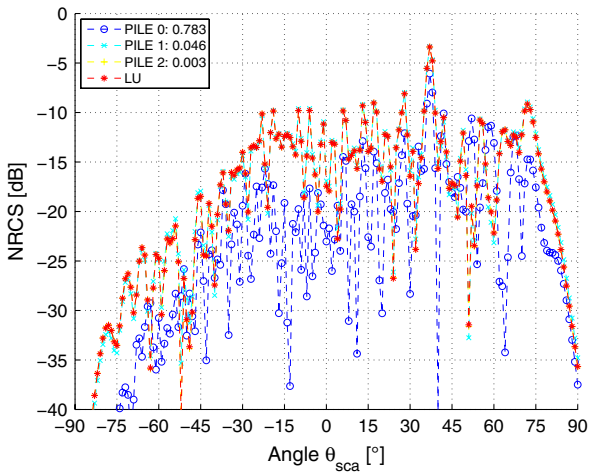

(b) Scenario 2 : NRCS.

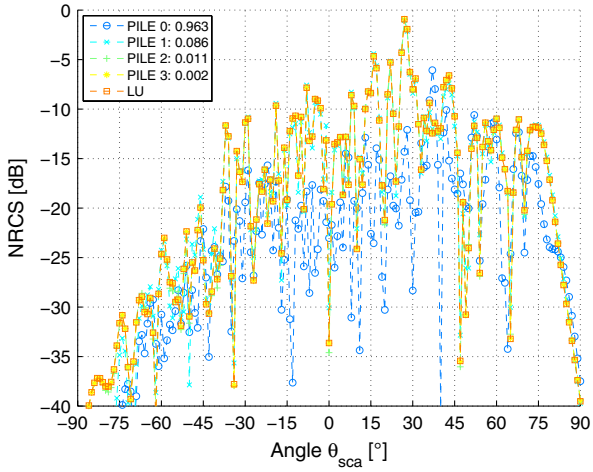

(c) Scenario 3 : NRCS.

Fig. 7. (a) RCS in dBm versus the scattering angle θ_{sca}; (b) NRCS in dB versus the scattering angle θ_{sca}; (c) NRCS in dB versus the scattering angle θ_{sca}. The parameters of the three scenarios are given in the caption of Fig. 6, and the polarization is TE.

$$\frac{\partial \psi_2(\boldsymbol{r})}{\partial n} = 2\begin{cases} \frac{\partial \psi_{\text{inc},1}(\boldsymbol{r})}{\partial n} & \boldsymbol{r} \in S_{2,\text{Ill}} \\ 0 & \boldsymbol{r} \in S_{2,\text{Sha}} \end{cases} \quad \text{and} \quad \psi_2(\boldsymbol{r}) = 0 \,\forall\, S_2, \text{TE polarization}, \tag{18}$$

where $\psi_{\text{inc},1}$ is the incident field in Ω_1 radiated from the surface currents on scatterer 1, $S_{2,\text{Ill}}$ stands for the illuminated surface, and $S_{2,\text{Sha}}$ for the shadowed surface ($S_2 = S_{2,\text{Ill}} \cup S_{2,\text{Sha}}$). Then, under the PO approximation, the inverse of the impedance matrix, $\bar{\boldsymbol{Z}}_2^{-1}$, is a diagonal matrix of elements $2(\bullet)$ for the TM polarization and of elements $2\partial(\bullet)/\partial n$ for the TE polarization. The complexity of the inversion is then $\mathcal{O}(1)$, instead of $\mathcal{O}(N_2^3)$ with a direct LU inversion.

Table 2. Values of the Norm $\|\bar{\boldsymbol{M}}_c\|$ of the Characteristic Matrix Defined by Eq. (13)

Polarization	Scenario 1	Scenario 2	Scenario 3
TE	0.2780	0.0735	0.1573
TM	0.5468	0.0746	0.1336

For example, for the calculation of $\boldsymbol{Y}_1^{(1)} = \bar{\boldsymbol{Z}}_1^{-1}\bar{\boldsymbol{Z}}_{21}\bar{\boldsymbol{Z}}_2^{-1}\bar{\boldsymbol{Z}}_{12}\boldsymbol{Y}_1^{(0)}$, where $\boldsymbol{Y}_1^{(0)} = \bar{\boldsymbol{Z}}_1^{-1}\boldsymbol{b}_1$, first, the vector $\boldsymbol{Y}_1^{(0)}$ is multiplied by the matrix $\bar{\boldsymbol{Z}}_{12}$, giving $u = \bar{\boldsymbol{Z}}_{12}\boldsymbol{Y}_1^{(0)}$. It can be considered as an incident field for scatterer 2. If PO is applied on scatterer 2, some elements of $\bar{\boldsymbol{Z}}_{12}$ can then be zero due to the fact that a point on scatterer 2 is not viewed from a point on scatterer 1. For a convex object, this condition is satisfied if $\hat{\boldsymbol{n}}_2 \cdot (\boldsymbol{r}_2 - \boldsymbol{r}_1) > 0$ [where $\boldsymbol{r}_{1,2} = (x_{1,2}, z_{1,2})$ is a point on scatterer (1, 2) and $\hat{\boldsymbol{n}}_2$ is the normal to the surface S_2 at the point $\boldsymbol{r}_2$ pointed toward the medium Ω_1]. Then, the elements of the modified matrix $\bar{\boldsymbol{Z}}'_{12}$ are

$$Z'_{12,mn} = Z_{12,mn}\frac{1-\mathrm{sgn}[(\boldsymbol{r}_{2,m}-\boldsymbol{r}_{1,n})\cdot\hat{\boldsymbol{n}}_{2,m}]}{2} = Z_{12,mn}\frac{1+\mathrm{sgn}[(x_{2,m}-x_{1,n})v_{2,m}\gamma_{2,m}-(z_{2,m}-z_{1,n})v_{2,m}]}{2}. \quad (19)$$

Next, $\boldsymbol{u} = \bar{\boldsymbol{Z}}_{12}\boldsymbol{Y}_1^{(0)}$ is multiplied by $\bar{\boldsymbol{Z}}_2^{-1}$. Then, if PO is applied on scatterer 2, the surface currents $\boldsymbol{v} = \bar{\boldsymbol{Z}}_2^{-1}\boldsymbol{u}$ are computed as follows:

$$\boldsymbol{v} = \bar{\boldsymbol{Z}}_2^{-1}\boldsymbol{u} = \bar{\boldsymbol{Z}}_2^{-1}\bar{\boldsymbol{Z}}'_{12}\boldsymbol{Y}_1^{(0)} = \bar{\boldsymbol{D}}\left[\bar{\boldsymbol{A}}'_{12}\frac{1}{\rho_{01}}\bar{\boldsymbol{B}}'_{12}\right]\begin{bmatrix}\boldsymbol{w}_1\\ \boldsymbol{w}_2\end{bmatrix} = \bar{\boldsymbol{D}}\left[\bar{\boldsymbol{A}}'_{12}\boldsymbol{w}_1 + \frac{1}{\rho_{01}}\bar{\boldsymbol{B}}'_{12}\boldsymbol{w}_2\right], \quad (20)$$

where $\bar{\boldsymbol{D}}$ is a diagonal matrix of elements $2(\bullet)$ for the TE polarization and of elements $2\partial(\bullet)/\partial n$ at the point $\boldsymbol{r}_2$. In addition, $\boldsymbol{Y}_1^{(0)} = [\boldsymbol{w}_1^T\boldsymbol{w}_2^T]^T$ ($\boldsymbol{w}_1$ and $\boldsymbol{w}_2$ are vectors of length N_1). For the TM polarization, the above equation requires us to compute $\partial\bar{\boldsymbol{A}}_{12}/\partial n$ and $\partial\bar{\boldsymbol{B}}_{12}/\partial n$ at the point $\boldsymbol{r}_2$. These computations are expressed in Appendix D.

B. Numerical Results

Figure 8 plots the RCS (in dBm) or the NRCS (in dB) versus the scattering angle θ_{sca} for a coated elliptical cylinder, an elliptical cylinder below a rough surface, and a rough layer. The polarization is TE, and the parameters of the scenarios are given in Fig. 6. In the legend, the labels are as follows:

– "PILE + LU + PO" means that PILE is hybridized with LU for the calculation of the local interactions on scatterer 1 and with PO for the calculation of the local interactions on scatterer 2.

– "PILE + FB + PO" means that PILE is hybridized with FB for the calculation of the local interactions on scatterer 1 and with PO for the calculation of the local interactions on scatterer 2.

– "PILE" means that PILE is not hybridized ("PILE + LU + LU").

– "LU" means that a direct LU inversion is applied.

In addition, the integer number after PILE between parentheses is the PILE order. It is chosen such that the residual error is smaller than 0.01. Last, the last number is the residual error computed from Eq. (16) by substituting the subscript

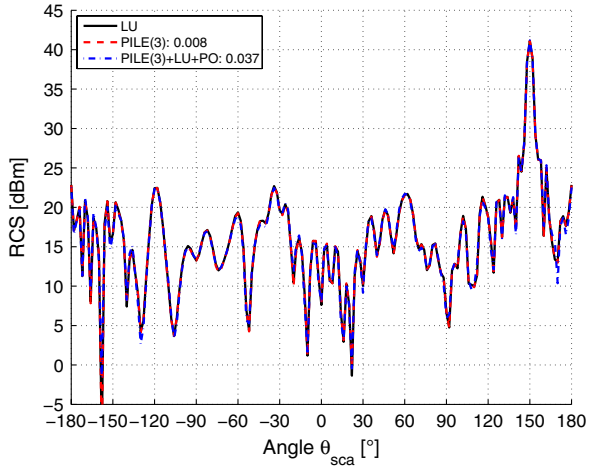

(a) Scenario 1 : RCS.

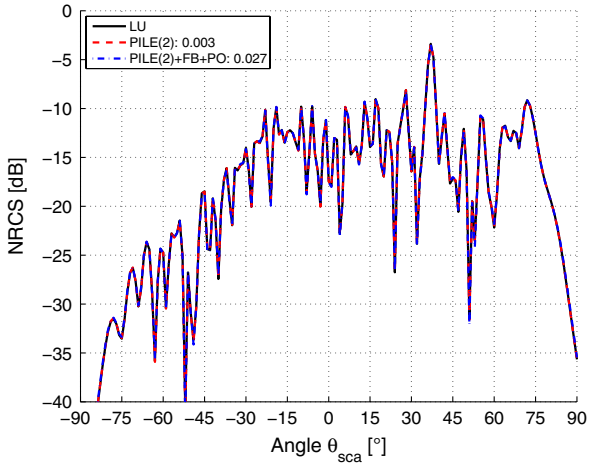

(b) Scenario 2 : NRCS.

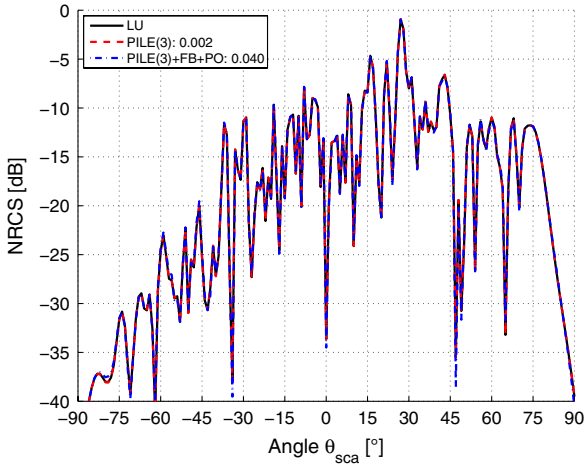

(c) Scenario 3 : NRCS.

Fig. 8. Same results as in Fig. 7, but the results with hybridization are added.

"PILE" by the chosen hybridization. When FB is applied, its order is determined from the study of the scattering from the single rough surface by choosing a residual error smaller than 0.01. For Figs. 8(b) and 8(c), $P_{\mathrm{FB}} = 7$.

As we can see in Fig. 8, a very good agreement is obtained between LU and the hybridization and the small difference in the residual error has a minor impact on the RCS or NRCS. Simulations for an incidence angle $\theta_{\mathrm{inc}} = 0$, not reported here, also showed very good agreements.

Figure 9 plots the computation time versus the number of unknowns. Scenario 1 is chosen, and to increase the number of unknowns, the problem size artificially increases by applying a scaling on the sizes of the cylinders. As the number of unknowns increases, Fig. 9 shows that PILE + LU + PO requires less computation time than LU and PILE + LU + LU. Due to the fact that the local interactions on the illuminated scatterer are computed from a direct LU inversion, the complexity for PILE + LU + PO is $\mathcal{O}(N_1^3)$. It is also important to note that the memory space requirement for PILE + LU + PO is smaller than for PILE + LU + LU, because the impedance matrix of the non-illuminated object is not computed (thus, not stored).

To study the limit of validity of PILE + LU + PO, we consider the scenario of Fig. 6(a) with the following changes: $a_1 = 2\lambda_0$, $a_2 = \lambda_0$, $b_1 = 2\lambda_0$, $b_2 = \lambda_0$ (smaller cylinders) and $C_1 = (-0.5, -0.5)\lambda_0$. In Fig. 10(a), the corresponding RCS is plotted versus θ_{sca}. We consider also the scenario of Fig. 6(c) with the following changes: $\sigma_{z2} = 0.5\lambda_0$ (rougher lower surface). The PO approximation is valid if the curvature radius of the surface r_{c0} is much larger than the wavelength λ_0 and if there are no multiple reflections, since PO is applied at the first order. More precisely, from [34], $r_{c0}\cos^3\theta_0 \gg \lambda_0$, where θ_0 is the local angle defined with respect to the normal to the surface.

For Fig. 10(a), $r_{c2} = \lambda_0$, which is smaller than that used in Fig. 8(a). In Fig. 10(a), this explains why the residual error is larger than that obtained in Fig. 8(a).

For Fig. 10(b), the mean of $r_{c2} = (1+\gamma_2^2)^{3/2}/|\gamma_2'|$, where $\gamma_2 = z_2'(x_2) = dz_2/dx_2$, is $\langle r_{c2}\rangle = 5.60$, whereas in Fig. 8(c), $\langle r_{c2}\rangle = 14.98$. In addition, for a random rough surface, the multiple reflections can be neglected if the surface slope standard deviation σ_s is smaller than 0.3. For Fig. 8(c), $\sigma_{s2} = 0.15$, whereas in Fig. 10(b), $\sigma_{s2} = 0.73$. This explains why the residual error is larger than that obtained in Fig. 8(c). A means to decrease the residual error is to apply the PO at the second order, meaning that the second reflection is accounted for. This procedure has been published to include the second reflection for the scattering from a PC dihedral located above a sea surface [30]. Then the complexity of programming and of the resulting method increase.

If a direct LU inversion is used, the method complexity is $\mathcal{O}((N_1+N_2)^3)$. For PILE + LU + LU, the complexity is similar. For PILE + LU + PO, the complexity becomes $\mathcal{O}(N_1^3)$ and the memory requirement is also reduced since the matrix $\bar{\bar{Z}}_2$ is not stored and the coupling matrix $\bar{\bar{Z}}_{12}$ is not full. For PILE + FB + PO, the complexity is reduced to $\mathcal{O}(N_1^2)$. For a detailed analysis of the complexity of PILE + FB – SA + FB – SA and PILE + FB – SA + LU, see [7] and [8], respectively.

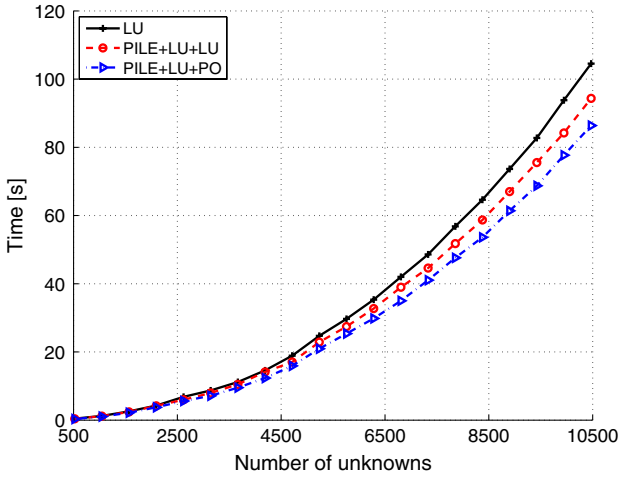

Fig. 9. Computation time versus the number of unknowns. Scenario 1 is chosen, and to increase the number of unknowns, the problem size artificially increases by applying a scaling on the sizes of the cylinders.

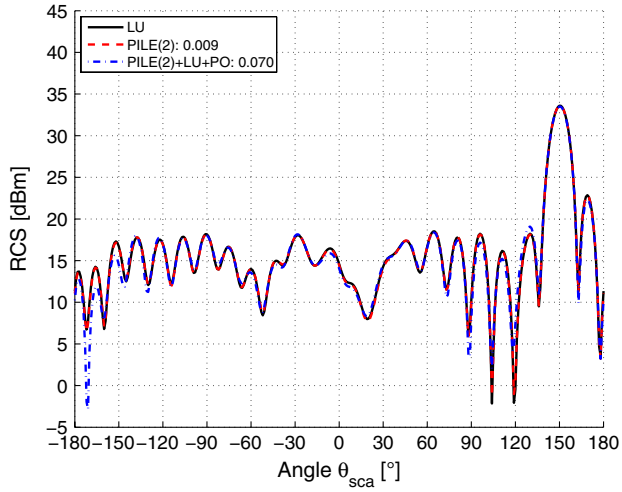

(a) Scenario 1 bis : RCS.

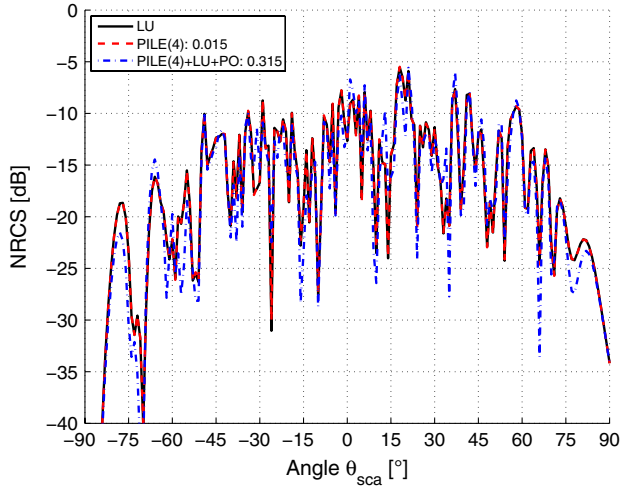

(b) Scenario 3 bis : NRCS.

Fig. 10. Same results as in Fig. 8, but with the following changes: (a) Fig. 10(a): scenario 1 of Fig. 6(a) but $a_1 = 2\lambda_0$, $a_2 = \lambda_0$, $b_1 = 2\lambda_0$, $b_2 = \lambda_0$ (smaller cylinders) and $C_1 = (-0.5, -0.5)\lambda_0$; (b) Fig. 10(b): Scenario 3 of Fig. 6(c) but $\sigma_{z2} = 0.5\lambda_0$ (rougher lower surface).

4. CONCLUSION

In this paper, from the integral equations to calculate the field scattered by two scatterers where only one is illuminated, an efficient numerical method has been presented. The PILE method is based on the MoM, and the impedance matrix of the two scatterers is then inverted by blocks from the Taylor series expansion of the inverse of the Schur complement. Furthermore, the PILE method allows one to use any fast method developed for a single interface. Here, for scatterer 2 assumed to be PC, to decrease the complexity of PILE, PO or/and FB have been hybridized with PILE, and according to the scenario, this hybridization gives satisfactory results. A prospect of this paper is to extend the hybridization to the case of a dielectric scatterer in order to reduce the complexity.

APPENDIX A: ELEMENTS OF THE MATRICES

In Eq. (5), the elements of the block matrices $\{\bar{\boldsymbol{A}}_1,\bar{\boldsymbol{B}}_1,\bar{\boldsymbol{C}}_1,\bar{\boldsymbol{D}}_1\}$ are expressed as

$$A_{1,mn}=\begin{cases}-\dfrac{jk_0v_n|\Delta_n|}{4}\dfrac{\mathrm{H}_1^{(1)}(k_0\|\boldsymbol{r}_n-\boldsymbol{r}_m\|)}{\|\boldsymbol{r}_n-\boldsymbol{r}_m\|}\times[\gamma_n(x_n-x_m)-(z_n-z_m)] & \text{for } m\neq n\\ +\dfrac{1}{2}-\dfrac{v_n|\Delta_n|}{4\pi}\dfrac{\gamma'(x_n)}{1+\gamma^2(x_n)} & \text{for } m=n\end{cases}, \tag{A1}$$

$$B_{1,mn}=\frac{j|\Delta_n|\sqrt{1+\gamma_n^2}}{4}\begin{cases}\left[1+\frac{2j}{\pi}\ln\left(0.164k_0\sqrt{1+\gamma_n^2}|\Delta_n|\right)\right] & \text{for } m=n\\ \mathrm{H}_0^{(1)}(k_0\|\boldsymbol{r}_n-\boldsymbol{r}_m\|) & \text{for } n\neq m\end{cases}, \tag{A2}$$

$$C_{1,mn}=\begin{cases}-\dfrac{jk_1v_n|\Delta_n|}{4}\dfrac{\mathrm{H}_1^{(1)}(k_1\|\boldsymbol{r}_n-\boldsymbol{r}_m\|)}{\|\boldsymbol{r}_n-\boldsymbol{r}_m\|}[\gamma_n(x_n-x_m)-(z_n-z_m)] & \text{for } m\neq n\\ -\dfrac{1}{2}-\dfrac{v_n|\Delta_n|}{4\pi}\dfrac{\gamma'(x_n)}{1+\gamma^2(x_n)} & \text{for } m=n\end{cases}, \tag{A3}$$

$$D_{1,mn}=\frac{j|\Delta_n|\sqrt{1+\gamma_n^2}}{4}\begin{cases}\left[1+\frac{2j}{\pi}\ln\left(0.164k_1\sqrt{1+\gamma_n^2}|\Delta_n|\right)\right] & \text{for } m=n\\ \mathrm{H}_0^{(1)}(k_1\|\boldsymbol{r}_n-\boldsymbol{r}_m\|) & \text{for } m\neq n\end{cases}, \tag{A4}$$

where $\boldsymbol{r}_n=(x_n,z_n)\in S_1$ (coordinates of the point on the surface S_1), $\boldsymbol{r}_m=(x_m,z_m)\in S_1$, $\gamma_n=dz_n/dx_n$, $\gamma_n'=d\gamma_n/dx_n$, Δ_n is the sampling step, $v_n=\mathrm{sgn}(\hat{\boldsymbol{n}}_n\cdot\hat{\boldsymbol{z}})$ (where $\hat{\boldsymbol{n}}_n$ is the normal vector to the point $\boldsymbol{r}_n$), $\mathrm{H}_0^{(1)}$ is the zeroth-order Hankel function of the first kind, and $\mathrm{H}_1^{(1)}$ is its derivative. The elements of the matrices $\{\bar{\boldsymbol{A}}_2,\bar{\boldsymbol{B}}_2,\bar{\boldsymbol{C}}_2,\bar{\boldsymbol{D}}_2\}$ are obtained from those of $\{\bar{\boldsymbol{A}}_1,\bar{\boldsymbol{B}}_1,\bar{\boldsymbol{C}}_1,\bar{\boldsymbol{D}}_1\}$ by substituting the wavenumbers $\{k_0,k_0,k_1,k_1\}$ for $\{k_1,k_1,k_2,k_2\}$, respectively.

The elements of the coupling matrices $\{\bar{\boldsymbol{A}}_{12},\bar{\boldsymbol{B}}_{12},\bar{\boldsymbol{A}}_{21},\bar{\boldsymbol{B}}_{21}\}$ are

$$\begin{cases}A_{12,mn}=-\dfrac{jk_1v_{1,n}|\Delta_{1,n}|}{4}\dfrac{\mathrm{H}_1^{(1)}(k_1\|\boldsymbol{r}_{1,n}-\boldsymbol{r}_{2,m}\|)}{\|\boldsymbol{r}_{1,n}-\boldsymbol{r}_{2,m}\|}\\ \qquad\times[\gamma_{1,n}(x_{1,n}-x_{2,m})-(z_{1,n}-z_{2,m})]\\ A_{21,mn}=-\dfrac{jk_1v_{2,n}|\Delta_{2,n}|}{4}\dfrac{\mathrm{H}_1^{(1)}(k_1\|\boldsymbol{r}_{2,n}-\boldsymbol{r}_{1,m}\|)}{\|\boldsymbol{r}_{2,n}-\boldsymbol{r}_{1,m}\|}\\ \qquad\times[\gamma_{2,n}(x_{2,n}-x_{1,m})-(z_{2,n}-z_{1,m})]\\ B_{12,mn}=\dfrac{j|\Delta_{1,n}|\sqrt{1+\gamma_{1,n}^2}}{4}\mathrm{H}_0^{(1)}(k_1\|\boldsymbol{r}_{1,n}-\boldsymbol{r}_{2,m}\|)\\ B_{21,mn}=\dfrac{j|\Delta_{2,n}|\sqrt{1+\gamma_{2,n}^2}}{4}\mathrm{H}_0^{(1)}(k_1\|\boldsymbol{r}_{2,n}-\boldsymbol{r}_{1,m}\|)\end{cases}. \tag{A5}$$

APPENDIX B: IMPEDANCE MATRIX WHEN SCATTERER 2 IS PC

If scatterer 2 is assumed to be PC, the impedance matrix $\bar{\boldsymbol{Z}}_2$ can be simplified. For the TE polarization (Dirichlet boundary condition), ψ_2 on the surface vanishes and the only unknown on the surface is $\partial\psi_2/\partial n$. Then

$$\mathrm{TE}:\bar{\boldsymbol{Z}}_2=\bar{\boldsymbol{B}}_2,\qquad \boldsymbol{X}_2=\frac{\partial\psi_2}{\partial n}. \tag{B1}$$

For the TM polarization (Neumann boundary condition), $\partial\psi_2/\partial n$ on the surface vanishes and the only unknown on the surface is ψ_2. Then

$$\mathrm{TM}:\bar{\boldsymbol{Z}}_2=\bar{\boldsymbol{A}}_2,\qquad \boldsymbol{X}_2=\psi_2. \tag{B2}$$

In addition, the coupling matrices are simplified as

$$\begin{cases}\mathrm{TE}:\bar{\boldsymbol{Z}}_{12}=\left[\bar{\boldsymbol{A}}_{12}\frac{1}{\rho_{01}}\bar{\boldsymbol{B}}_{12}\right],\quad \bar{\boldsymbol{Z}}_{21}=\begin{bmatrix}\bar{\boldsymbol{0}}\\ \bar{\boldsymbol{B}}_{21}\end{bmatrix}\\ \mathrm{TM}:\bar{\boldsymbol{Z}}_{12}=\left[\bar{\boldsymbol{A}}_{12}\frac{1}{\rho_{01}}\bar{\boldsymbol{B}}_{12}\right],\quad \bar{\boldsymbol{Z}}_{21}=\begin{bmatrix}\bar{\boldsymbol{0}}\\ \bar{\boldsymbol{A}}_{21}\end{bmatrix}\end{cases}. \tag{B3}$$

APPENDIX C: ANALYTICAL SOLUTION OF A COATED CIRCULAR CYLINDER

This appendix briefly presents the field scattered by a coated circular cylinder (two concentric circular cylinders) and computed in polar coordinates (r,θ), where the angle θ is defined from the horizontal axis $\hat{\boldsymbol{x}}$. An incident plane wave is considered: $\psi_{\text{inc}}=\psi_{\text{inc},0}e^{jk_0(x\sin\theta_{\text{inc}}-z\cos\theta_{\text{inc}})}=\psi_{\text{inc},0}e^{jk_0r\sin(\theta_{\text{inc}}-\theta)}$ $[\boldsymbol{k}_0=\boldsymbol{k}_0(\hat{\boldsymbol{x}}\sin\theta_{\text{inc}}-\hat{\boldsymbol{z}}\cos\theta_{\text{inc}})]$ with $\tan\theta=z/x$ and $r=\sqrt{x^2+z^2}$.

In media Ω_0, Ω_1, and Ω_2, the total fields are

$$\psi_0(r,\theta)=\sum_{n=-\infty}^{n=+\infty}[A_nJ_n(k_0r)+B_n\mathrm{H}_n^{(1)}(k_0r)]e^{-jn\theta}\quad\text{with}$$
$$A_n=\psi_{\text{inc},0}e^{jn\theta_{\text{inc}}},\tag{C1}$$

$$\psi_1(r,\theta)=\sum_{n=-\infty}^{n=+\infty}[C_nJ_n(k_1r)+D_n\mathrm{H}_n^{(1)}(k_1r)]e^{-jn\theta},\tag{C2}$$

$$\psi_2(r,\theta)=\sum_{n=-\infty}^{n=+\infty}E_nJ_n(k_2r)e^{-jn\theta},\tag{C3}$$

respectively, where $\mathrm{H}_n^{(1)}$ is the nth-order Hankel function of the first kind and J_n is the nth-order Bessel function of the first kind. In Eqs. (C1)–(C3), the four unknowns are B_n, C_n, D_n, and E_n. The boundary conditions state that

$$\begin{cases}\psi_0(a_1,\theta)=\psi_1(a_1,\theta)\\ \psi_1(a_2,\theta)=\psi_2(a_2,\theta)\\ \dfrac{\partial\psi_0}{\partial r}\Big|_{r=a_1}=\rho_{01}\dfrac{\partial\psi_1}{\partial r}\Big|_{r=a_1}\\ \dfrac{\partial\psi_1}{\partial r}\Big|_{r=a_2}=\rho_{12}\dfrac{\partial\psi_2}{\partial r}\Big|_{r=a_2}\end{cases}.\tag{C4}$$

From Eqs. (C1)–(C3), this leads for any (θ,n) to

$$\begin{bmatrix}\mathrm{H}_n^{(1)}(k_0a_1) & -J_n(k_1a_1) & -\mathrm{H}_n^{(1)}(k_1a_1) & 0\\ k_0\mathrm{H}_n'^{(1)}(k_0a_1) & -\rho_{01}k_1J_n'(k_1a_1) & -\rho_{01}k_1\mathrm{H}_n'^{(1)}(k_1a_1) & 0\\ 0 & J_n(k_1a_2) & \mathrm{H}_n^{(1)}(k_1a_2) & -J_n(k_2a_2)\\ 0 & k_1J_n'(k_1a_2) & k_1\mathrm{H}_n'^{(1)}(k_1a_2) & -k_2\rho_{12}J_n'(k_2a_2)\end{bmatrix}\begin{bmatrix}B_n\\C_n\\D_n\\E_n\end{bmatrix}=\begin{bmatrix}-A_nJ_n(k_0a_1)\\-A_nk_0J_n'(k_0a_1)\\0\\0\end{bmatrix}.\tag{C5}$$

This linear system can be solved analytically or numerically by inverting the matrix of size 4×4. The RCS in medium Ω_0 is then expressed as

$$\mathrm{RCS}(\theta_{\text{inc}},\theta_{\text{sca}})=\frac{4}{k_0}\left|\sum_{n=-\infty}^{n=+\infty}B_ne^{jn(\theta_{\text{inc}}+\theta_{\text{sca}}-\pi)}\right|^2.\tag{C6}$$

APPENDIX D: DERIVATION OF THE COUPLING MATRICES FOR PO

From Eq. (5), we show that

$$\left.\frac{\partial B_{12,mn}}{\partial n}\right|_{\mathbf{r}_{2,m}}=\frac{jk_1v_{2,m}|\Delta_{1,n}|\sqrt{1+\gamma_{1,n}^2}\mathrm{H}_{11}}{4r_{12}\sqrt{1+\gamma_{2,m}^2}}(z_{12}-\gamma_{2,m}x_{12})\tag{D1}$$

and

$$\left.\frac{\partial A_{12,mn}}{\partial n}\right|_{\mathbf{r}_{2,m}}=-\frac{jk_1v_{1,n}|\Delta_{1,n}|v_{2,m}}{4\sqrt{1+\gamma_{2,m}^2}}[w_{00}+w_{10}(\gamma_{1,n}+\gamma_{2,m})+w_{11}\gamma_{1,n}\gamma_{2,m}],\tag{D2}$$

where

$$\begin{cases}w_{00}=\dfrac{k_1z_{12}^2\mathrm{H}_{10}}{r_{12}^2}+\dfrac{(x_{12}^2-z_{12}^2)\mathrm{H}_{11}}{r_{12}^3}\\ w_{10}=\dfrac{x_{12}z_{12}}{r_{12}^3}(2\mathrm{H}_{11}-\mathrm{H}_{10}k_1r_{12})\\ w_{11}=\dfrac{k_1x_{12}^2\mathrm{H}_{10}}{r_{12}^2}+\dfrac{(z_{12}^2-x_{12}^2)\mathrm{H}_{11}}{r_{12}^3}\end{cases},\tag{D3}$$

and $x_{12}=x_{1,n}-x_{2,m}$, $z_{12}=z_{1,n}-z_{2,m}$, $r_{12}=\sqrt{x_{12}^2+z_{12}^2}$, $\mathrm{H}_{10}=\mathrm{H}_0^{(1)}(k_1r_{12})$, $\mathrm{H}_{11}=\mathrm{H}_1^{(1)}(k_1r_{12})$.

REFERENCES

1. J. T. Johnson, "A numerical study of scattering from an object above a rough surface," IEEE Trans. Antennas Propag. **50**, 1361–1367 (2002).
2. D. E. Lawrence and K. Sarabandi, "Electromagnetic scattering from a dielectric cylinder buried beneath a slightly rough surface," IEEE Trans. Antennas Propag. **50**, 1368–1376 (2002).
3. X. Wang, C.-F. Wang, Y.-B. G. Gan, and L.-W. Li, "Electromagnetic scattering from a circular target above or below rough surface," Progr. Electromagn. Res. **40**, 207–227 (2003).
4. N. Déchamps, N. De Beaucoudrey, C. Bourlier, and S. Toutain, "Fast numerical method for electromagnetic scattering by rough layered interfaces: propagation-inside-layer expansion method," J. Opt. Soc. Am. A **23**, 359–369 (2006).
5. C.-H. Kuo and M. Moghaddam, "Electromagnetic scattering from a buried cylinder in layered media with rough interfaces," IEEE Trans. Antennas Propag. **54**, 2392–2401 (2006).
6. N. Déchamps and C. Bourlier, "Electromagnetic scattering from a rough layer: propagation-inside-layer expansion method combined to an updated BMIA/CAG approach," IEEE Trans. Antennas Propag. **55**, 2790–2802 (2007).

7. N. Déchamps and C. Bourlier, "Electromagnetic scattering from a rough layer: propagation-inside-layer expansion method combined to the forward-backward novel spectral acceleration," IEEE Trans. Antennas Propag. **55**, 3576–3586 (2007).
8. C. Bourlier, G. Kubické, and N. Déchamps, "A fast method to compute scattering by a buried object under a randomly rough surface: PILE combined to FB-SA," J. Opt. Soc. Am. A **25**, 891–902 (2008).
9. S. Ahmed and Q. A. Naqvi, "Electromagnetic scattering from a perfect electromagnetic conductor cylinder buried in a dielectric half-space," Progr. Electromagn. Res. **78**, 25–38 (2008).
10. F. Frezza, C. Pajewski, C. Ponti, and G. Schettini, "Scattering by dielectric circular cylinders in a dielectric slab," J. Opt. Soc. Am. A **27**, 687–695 (2010).
11. P. Pawliuk and M. Yedlin, "Scattering from cylinders using the two-dimensional vector plane wave spectrum," J. Opt. Soc. Am. A **28**, 1177–1184 (2011).
12. A. F. Fiaz, F. Frezza, L. Pajewski, C. Ponti, and G. Schettini, "Scattering by a circular cylinder buried under a slightly rough surface: the cylindrical-wave approach," IEEE Trans. Antennas Propag. **60**, 2834–2842 (2012).
13. G. P. Zouros, "Electromagnetic plane wave scattering by arbitrarily oriented elliptical dielectric cylinders," J. Opt. Soc. Am. A **28**, 2376–2384 (2011).
14. S.-C. Lee, "Scattering by closely spaced parallel non homogeneous cylinders in an absorbing medium," J. Opt. Soc. Am. A **28**, 1812–1819 (2011).
15. G. P. Zouros, "Oblique electromagnetic scattering from lossless or lossy composite elliptical dielectric cylinders," J. Opt. Soc. Am. A **30**, 196–205 (2013).
16. M. A. Fiaz, F. Frezza, L. Pajewski, C. Ponti, and G. Schettini, "Asymptotic solution for a scattered field by cylindrical objects buried beneath a slightly rough surface," Near Surf. Geophysics **11**, 177–183 (2013).
17. D. A. Kapp and G. S. Brown, "A new numerical method for rough-surface scattering calculations," IEEE Trans. Antennas Propag. **44**, 711–722 (1996).
18. R. J. Adams and G. S. Brown, "An iterative solution of one-dimensional rough surface scattering problems based on a factorization of the Helmholtz operator," IEEE Trans. Antennas Propag. **47**, 765–767 (1996).
19. D. Holliday, L. L. DeRaad, Jr., and G. J. St-Cyr, "Forward–backward method for scattering from imperfect conductors," IEEE Trans. Antennas Propag. **46**, 101–107 (1998).
20. A. Iodice, "Forward–backward method for scattering from dielectric rough surfaces," IEEE Trans. Antennas Propag. **50**, 901–911 (2002).
21. H. T. Chou and J. T. Johnson, "A novel acceleration algorithm for the computation of scattering from rough surfaces with the forward–backward method," Radio Sci. **33**, 1277–1287 (1998).
22. H. T. Chou and J. T. Johnson, "Formulation of the forward-backward method using novel spectra acceleration for the modeling of scattering from impedance rough surfaces," IEEE Trans. Geosci. Remote Sens. **38**, 605–607 (2000).
23. D. Torrungrueng, H. T. Chou, and J. T. Johnson, "A novel acceleration algorithm for the computation of scattering from two-dimensional large-scale perfectly conducting random rough surfaces with the forward-backward method," IEEE Trans. Geosci. Remote Sens. **38**, 1656–1668 (2000).
24. D. Torrungrueng, J. T. Johnson, and H. T. Chou, "Some issues related to the novel spectral acceleration method for the fast computation of radiation/scattering from one-dimensional extremely large scale quasi-planar structures," Radio Sci. **37** (2):3, 1–20 (2002).
25. L. Tsang, C. H. Chang, and H. Sangani, "A banded matrix iterative approach to Monte Carlo simulations of scattering of waves by large scale random rough surface problems: TM case," Electron. Lett. **29**, 1666–1667 (1993).
26. L. Tsang, C. H. Chang, H. Sangani, A. Ishimaru, and P. Phu, "A banded matrix iterative approach to monte carlo simulations of large scale random rough surface scattering: TE case," J. Electromagn. Waves Appl. **29**, 1185–1200 (1993).
27. L. Tsang, C. H. Chang, K. Pak, and H. Sangani, "Monte-Carlo simulations of large-scale problems of random rough surface scattering and applications to grazing incidence with the BMIA/canonical grid method," IEEE Trans. Antennas Propag. **43**, 851–859 (1995).
28. G. Kubické, C. Bourlier, and J. Saillard, "Scattering by an object above a randomly rough surface from a fast numerical method: extended PILE method combined to FB-SA," IEEE Trans. Antennas Propag. **18**, 495–519 (2008).
29. G. Kubické, C. Bourlier, and J. Saillard, "Scattering from canonical objects above a sea-like 1D rough surface from a rigorous fast method," Waves Random Complex Media **20**, 156–178 (2010).
30. G. Kubické and C. Bourlier, "A fast hybrid method for scattering from a large object with dihedral effects above a large rough surface," IEEE Trans. Antennas Propag. **59**, 189–198 (2011).
31. W. H. Press, S. A. Teutolsky, W. T. Vetterling, and B. P. Flannery, *Numerical Recipies*, 2nd ed. (Cambridge University, 1992).
32. E. I. Thorsos, "The validity of the Kirchhoff approximation for rough surface scattering using a Gaussian roughness spectrum," J. Acoust. Soc. Am. **83**, 78–92 (1988).
33. L. Tsang, J. A. Kong, K.-H. Ding, and C. O. Ao, *Scattering of Electromagnetic Waves: Numerical Simulations* (Wiley, 2000).
34. L. M. Brekhovskikh, *Waves in Layered Media*, 2nd ed. (Academic, 1980).